Check for updates

Catalytic oxidation of NO over MnOx–CoOx/TiO2 in the presence of a low ratio of O3/NO: activity and mechanism†

Meng Si, [ID] [a] Boxiong Shen,*[a] Lijun Liu,[a] Haohao Zhang,[a] Wenjun Zhou,[a] Jianqiao Wang,[a] Xiao Zhang,[a] Zhikun Zhang[a] and Chunfei Wu[b]

In order to broaden the temperature range of NO oxidation reaction in flue gas and maintain high oxidation efficiency, various loading amounts of MnO_x–CoO_x/TiO_2 mesoporous catalysts were tested in the catalytic oxidation of NO. It was found that 15%MnO_x–CoO_x(2 : 1)/TiO_2 demonstrated the best adsorption performance to oxygen species and contained more oxygen vacancies, as well as the best surface oxygen mobility, thus exhibiting excellent NO catalytic oxidation activity. O_3 (O_3/NO < 1) combined with 15%MnO_x–CoO_x(2 : 1)/TiO_2 improved the oxidation efficiency of NO at 50–400 °C, especially below 250 °C. When the temperatures were less than 250 °C, the oxidation efficiencies of NO by O_3 over 15% MnO_x–CoO_x(2 : 1)/TiO_2 were 5–13% higher than the calculated theoretical efficiencies. This indicated that there was a synergistic effect between O_3 and 15%MnO_x–CoO_x(2 : 1)/TiO_2 below 250 °C. Based on the results of *in situ* DRIFTS studies, it was deduced that monodentate nitrates were the main intermediates that produced a synergistic effect due to the introduction of O_3. In addition, O_3 accelerated the transformation between nitrate species, decreased the decomposition temperature of nitrate species, and inhibited the accumulation of nitrate ions, thus improving the oxidation efficiency of NO.

1. Introduction

NO_x (including NO and NO_2) are major pollutants emitted from fossil fuel combustion. In the last two decades, there has been much concern on techniques to control NO_x emission. Selective catalytic reduction and selective non-catalytic reduction are widely used in industry,[1] but the problems of high reaction temperature requirement, NH_3 escape in flue gas, and difficulty in removing low concentrations of NO_x still exist.[2–4] In recent years, the oxidation technology of NO to NO_2 has received attention.[5–8] In particular, the applications of transition metal oxides to catalytic oxidation of NO were studied.[9–12] Among them, MnO_x and CoO_x have been reported to show good activity for NO catalytic oxidation. Qiu[13] prepared Mn–Co/TiO_2 catalysts with different loadings by wet impregnation method. Their results indicated that the efficiency of NO oxidation by O_2 was the best using 10Mn–5Co/TiO_2 (loading ratio of Mn was 10 wt%

and Co was 5 wt%) at 300 °C. Li[14] found that the interaction between Co and Mn promoting the generation of Mn_2O_3 improved the NO oxidation by O_2 above 250 °C. Nevertheless, the catalytic oxidation of NO by catalysts combined with oxygen is inefficient when the temperature was below 150 °C. To obtain higher efficiency of NO oxidation at low temperature, ozone has been widely used considering the lower secondary pollutants.[6,15] Jõgi[16] reported the NO oxidation by ozone over TiO_2 catalyst and Lin[17] reported the NO oxidation by O_3 combined with MnO_x catalyst supported by spherical alumina. It is agreed in these papers that when the temperature was less than 200 °C and the molar ratio of O_3/NO < 1, the catalysts had no promoting effect on NO oxidation by O_3, and the oxidation efficiency of NO to NO_2 was the same as that when ozone oxidized NO alone. When the ratio of O_3/NO was greater than 1, the presence of catalysts could promote the deep oxidation of NO_2 to N_2O_5 by O_3 and reduce the consumption of ozone. However, higher O_3/NO_x could result in the leakage of ozone and the increase in capital cost. Therefore, NO oxidation by catalysts combined with low concentration of O_3 has become a new research target. Han[18] found that black-TiO_2 catalyst could increase the removal rate of NO in ozonation system at 60 °C when O_3/NO = 0.6. However, so far, there have been few reports about the NO catalytic oxidation mechanism with low molar ratios of O_3 to NO.

In this study, MnO_x–CoO_x/TiO_2 catalysts with different loadings were prepared with 2 : 1 molar ratio of Mn to Co. The

[a]Tianjin Key Laboratory of Clean Energy and Pollutant Control, School of Energy and Environmental Engineering, Hebei University of Technology, Tianjin 300401, China. E-mail: shenbx@hebut.edu.cn; 1253757136@qq.com; 1120136367@qq.com; 834295039@qq.com; 540885294@qq.com; 827179578@qq.com; 626855264@qq.com; 524591963@qq.com; Tel: +86-022-60435784

[b]School of Chemistry and Chemical Engineering, Queen's University of Belfast, Belfast, Northern Ireland, UK. E-mail: c.wu@qub.ac.uk

† Electronic supplementary information (ESI) available. See DOI: 10.1039/d0ra04129g

performance of these catalysts was investigated in NO catalytic oxidation. The optimum catalyst was selected for the research of NO oxidation by low molar ratios of O_3/NO (O_3/NO < 1) at 50–400 °C. A series of characterization techniques, such as N_2 adsorption, X-ray diffraction (XRD), thermogravimetric-differential scanning calorimetry (TG-DSC), H_2-temperature program reduction (H_2-TPR), O_2-temperature program desorption (O_2-TPD) and X-ray photoelectron spectroscopy (XPS), were used to identify the physicochemical characteristics of the catalysts. The technology of *in situ* DRIFTS was introduced to explore the promotion mechanism of NO oxidation by low concentration of O_3 in presence of MnO_x–CoO_x/TiO_2.

2. Materials and methods

2.1 Catalyst preparation

The catalysts were prepared by impregnation method. Specific amounts of manganese nitrate solution (50 wt%, analytical grade) and $Co(NO_3)_2 \cdot 6H_2O$ crystals (99 wt%, analytical grade) were added into 100 mL deionized water and the mixture was stirred for 30 min. A certain amount of anatase TiO_2 powder (commercial anatase titanium dioxide) was added into the solution and stirring was continued for 2 hours. Then, the mixture was heated in a thermostatic water bath at 80 °C until the water was fully evaporated. The catalyst precursors were dried at 110 °C for 12 hours, and then calcined under air atmosphere at 500 °C for 4 hours. The calcined catalysts were ground to 40–60 mesh size for the activity tests. For the as-prepared MnO_x–CoO_x supported catalysts, the molar ratio of Mn to Co was 2 : 1 and total loadings of Mn and Co to TiO_2 were 7 wt%, 10 wt%, 15 wt% and 20 wt%. Accordingly, they were denoted as 7%MnO_x–CoO_x(2 : 1)/TiO_2, 10%MnO_x–CoO_x(2 : 1)/TiO_2, 15%MnO_x–CoO_x(2 : 1)/TiO_2 and 20%MnO_x–CoO_x(2 : 1)/TiO_2, respectively.

2.2 Catalyst characterization

The specific surface areas and pore size distributions were determined by N_2 adsorption at liquid nitrogen temperature 77 K using a Micromeritics ASAP 2020 HD88 instrument. XRD patterns were recorded by a D8 FOCUS X-ray diffractometer (Bruker) with Cu Kα radiation operated at 40 kV and 40 mA. TGA curves were recorded on a TA-Q600 analyzer over the temperature range from 20 °C to 1000 °C at the rate of 10 °C min^{-1} under N_2. H_2-TPR, O_2-TPD and NO-TPD were carried out on PCA-1200 chemical adsorption instrument with a thermal conductivity detector. For H_2-TPR, samples were pretreated at 200 °C for 90 min in nitrogen atmosphere, then cooled down to room temperature. Catalysts were flushed in a flow of H_2 (5%)/N_2 and then heated to 900 °C at a rate of 10 °C min^{-1}. The H_2 consumption of the test samples were calculated by the H_2 consumption of 50 mg of CuO under the same reaction conditions. For O_2-TPD, catalysts were purged at room temperature for 30 min and then at 200 °C for 2 h in He atmosphere. Subsequently, O_2 was adsorbed at 100 °C for 1 h. The adsorbed catalyst was blown by He for 30 min at 100 °C, and then raised to 900 °C in He atmosphere (30 mL min^{-1}) at a rate of 10 °C min^{-1}.

The O_2 desorption quantity of each sample was calculated by standard pulse peak calibration method. For NO-TPD, catalysts were purged at 300 °C for 1 h in He atmosphere and then cooled down to room temperature. Subsequently, NO was adsorbed at room temperature for 1 h. The adsorbed catalysts were blown by He for 1 h at room temperature, and then raised to 500 °C in He atmosphere (30 mL min^{-1}) at a rate of 10 °C min^{-1} for desorption experiments. Desorption signals were detected by a thermal conductivity detector. XPS data were collected using a ThermoScientific Escalab 250Xi photoelectron spectrometer with a standard Al Kα source ($h\nu$ = 1486.6 eV). All binding energies were referenced to the C 1s line at 284.8 eV.

2.3 Catalytic tests

Activity tests of catalysts were carried out at 50–400 °C in a fixed-bed reactor that was 0.8 cm in diameter and 20 cm in length; the experimental system is shown in Fig. S1.† The simulated flue gases included 500 ppm NO, 4% O_2 and N_2 as carrier. O_3 was generated from O_2-ozone generator (SK-CFG-10A, 1–10 g h^{-1}, Sankang, Jinan, China), and was monitored by ozone detector (GM-6000-OEM, 0–200 g m^{-3}, Anseros, Germany). The molar ratio of O_3/NO was 0.1 to 0.9. The total gas flow rate was 400 mL min^{-1} with a gaseous hourly space velocity (GHSV) of 24 000 h^{-1}. The inlet and outlet NO concentrations were determined by flue gas analyzer (KM940, Kane, UK). The conversion efficiency of NO was calculated by eqn (1):

$$\text{NO oxidation efficiency} = \frac{\text{NO}_{\text{inlet}} - \text{NO}_{\text{outlet}}}{\text{NO}_{\text{inlet}}} \times 100\% \quad (1)$$

where NO_{inlet} and NO_{outlet} denote the inlet and outlet NO concentrations (ppm), respectively.

2.4 *In situ* DRIFTS

In situ diffuse reflectance infrared Fourier transform spectroscopy (DRIFTS) was performed using a Bruker Tensor II instrument and Harrick Scientific DRIFTS cell with ZnSe windows. The total gas flow rate was 200 mL min^{-1} containing 500 ppm NO, 250 ppm O_3, 4% O_2 and N_2 as carrier. The samples were pretreated under N_2 atmosphere in DRIFTS cell at 400 °C for 1 h, and then cooled down to the target temperature to collect the background spectra. The spectra of NO_x desorption as a function of temperature (25–400 °C) were recorded. The simultaneous adsorption data of NO and O_3 or NO and O_2 on 15% MnO_x–CoO_x(2 : 1)/TiO_2 as a function of time were recorded at 100 °C and 350 °C, respectively. Static reaction spectra without fed gases, after NO and O_3 co-adsorbed on 15%MnO_x–CoO_x(2 : 1)/TiO_2 at 100 °C, was also recorded.

3. Results and discussion

3.1 Catalyst characterization

3.1.1 N_2 adsorption analysis. The results of N_2 adsorption analysis of MnO_x–CoO_x(2 : 1)/TiO_2 catalysts with different loading amounts are shown in Fig. 1. The BET surface area, total pore volume and average pore width decreased with the increase in total loading amount (listed in Table 1). It was found
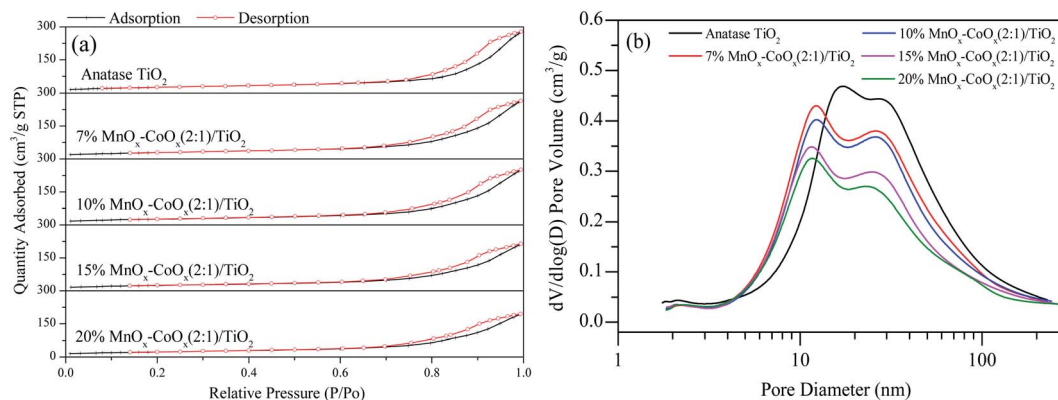
Fig. 1 (a) N_2 adsorption–desorption curves and (b) pore size distribution curves of MnO_x–$CoO_x(2:1)/TiO_2$.

that N_2 adsorption and desorption isotherm curves (shown in Fig. 1(a)) were inconsistent at high P/P_0 (>0.6). The curves belonged to a typical type IV isotherm, which indicated that these catalysts were all mesoporous materials. The catalysts exhibited a uniform pore size distribution with a mesoporous developed pore structure. The increase in catalyst loading amount resulted in a slight decrease in pore size distribution (shown in Fig. 1(b)).

3.1.2 TG-DSC analysis. Fig. 2 shows the results of TG-DSC analysis. All the catalysts showed a significant weight loss at around 600 °C. Four decalescence points were observed on 15% MnO_x–$CoO_x(2:1)/TiO_2$ from the DSC curves, but other catalysts had three. The decalescence points less than 100 °C indicated the evaporation of the remaining water in the catalysts. The wide decalescence valleys from 500 °C to 700 °C represented the transformation of MnO_2 to Mn_2O_3, and the decalescence valleys from 700 °C to 850 °C represented the transformation of Mn_2O_3 to Mn_3O_4.[19–21] In the DSC curve of 15%MnO_x–$CoO_x(2:1)/TiO_2$ at 271 °C, there was a decalescence point and a weight-loss point, which indicated that Co_2O_3 hydrate was dehydrated to Co_3O_4.[20] The continuous weight-loss from room temperature to approximately 600 °C confirmed that most of MnO_2 probably existed in amorphous form and only a small amount of it might exist as crystallites.[19]

3.1.3 XRD analysis. XRD patterns were recorded to determine the crystal phases of the four catalysts and TiO_2 carrier. As shown in Fig. 3, the distinct diffraction peaks of anatase TiO_2 crystal (ICDD 01-089-4921) were detected on each catalyst and no characteristic peaks of CoO_x were found. However, very weak

characteristic peaks of Mn_2O_3 were detected on 15%MnO_x–$CoO_x(2:1)/TiO_2$ and 20%MnO_x–$CoO_x(2:1)/TiO_2$ with higher loading of Mn oxides, and no diffraction peaks of MnO_2 were detected. Combined with the results of TG-DSC analysis, it could be speculated that the crystallinity of MnO_2 on the catalyst was very low and might exist primarily in an amorphous form. Manganic oxide species and cobalt oxide species were well-dispersed on the surface of catalysts and/or had poor crystal structure,[22] which would be beneficial to the catalytic reaction.[23] Average grain sizes calculated by the most intense reflexion characterizing of anatase TiO_2 using Scherrer formula are listed in Table 1. Decrease in average grain size of anatase TiO_2 carrier with the increase in loading of MnO_x–CoO_x was probably due to that the increase in active components was not conducive to the agglomeration of the carrier crystal.

3.1.4 H_2-TPR analysis. The results of H_2-TPR of the catalysts are displayed in Fig. 4. TiO_2 carrier exhibited a reduction peak at 611 °C. For 7%MnO_x–$CoO_x(2:1)/TiO_2$ and 10%MnO_x–$CoO_x(2:1)/TiO_2$, two reduction peaks were observed at 332 °C and 490 °C. The results of TG-DSC indicating MnO_2 was present in the catalysts. According to the comparison of single supported catalyst and manganese cobalt co-supported catalyst in Fig. S3,† reduction peak at 332 °C could be assigned to the reduction of MnO_2 to Mn_2O_3,[19] and Co_3O_4 to CoO.[20] The reduction peak at 490 °C was due to the reduction of Mn_2O_3 occurred through Mn_3O_4 to MnO (ref. 24) and the reduction of CoO to Co.[20] The interaction among metals might cause the reduction peaks changed in temperature or be covered by other peaks. For 15%MnO_x–$CoO_x(2:1)/TiO_2$ and 20%MnO_x–

Table 1 Physical parameters of catalysts

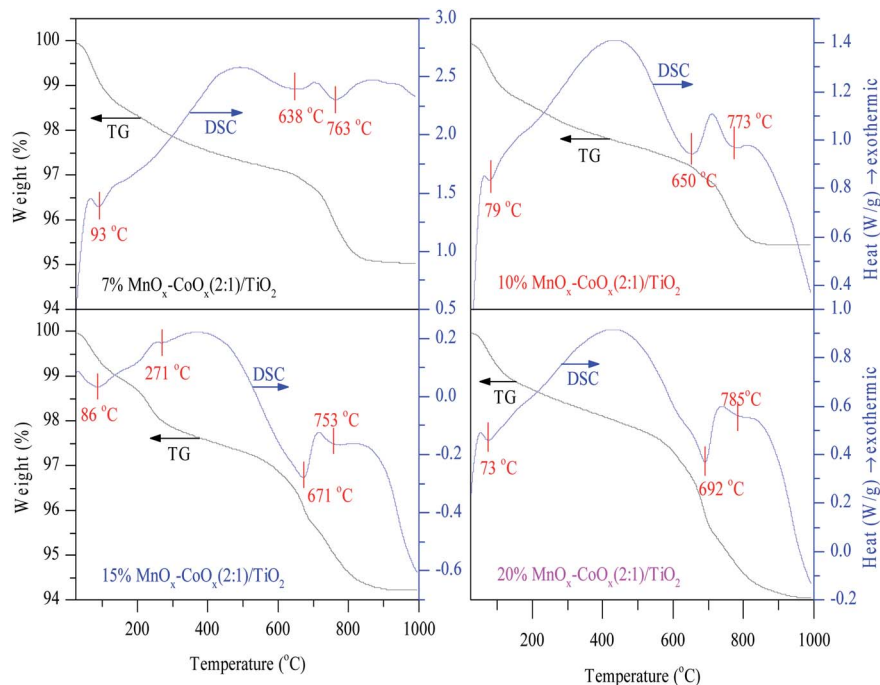| Catalyst	BET surface area ($m^2\ g^{-1}$)	Total pore volume ($cm^3\ g^{-1}$)	Average pore width (nm)	Average grain size (Å)
TiO_2	102.90	0.43	18.26	211
7%MnO_x–$CoO_x(2:1)/TiO_2$	95.86	0.41	16.13	156
10%MnO_x–$CoO_x(2:1)/TiO_2$	94.47	0.39	15.90	155
15%MnO_x–$CoO_x(2:1)/TiO_2$	88.29	0.33	15.02	152
20%MnO_x–$CoO_x(2:1)/TiO_2$	82.04	0.30	14.70	149

Fig. 2 TG-DSC profiles of catalysts.

$CoO_x(2 : 1)/TiO_2$, the reduction peak at 350 °C corresponded to the reduction of MnO_2 to Mn_2O_3 and Co_3O_4 to CoO. According to Fig. S3,† the peak at 511 °C with a shoulder peak at 533 °C and the peak at 515 °C with a shoulder peak at 543 °C could be ascribed to the reduction of CoO to Co and the reduction of Mn_2O_3 occurred through Mn_3O_4 to MnO.[19,20] The reduction temperatures of Mn_2O_3 and CoO on $15\%MnO_x$–$CoO_x(2 : 1)/TiO_2$ catalyst were slightly lower than those of $20\%MnO_x$–$CoO_x(2 : 1)/TiO_2$, which meant that the reduction of Mn_2O_3 and CoO on $15\%MnO_x$–$CoO_x(2 : 1)/TiO_2$ occurred easilier when compared to that of $20\%MnO_x$–$CoO_x(2 : 1)/TiO_2$. As shown in Table 2, the consumption of H_2 gradually increased as the loading amount

increased, reflecting the improvement of redox performance with the increase in loading amount.

3.1.5 O_2-TPD analysis. O_2-TPD results of the different loaded catalysts and TiO_2 carrier are shown in Fig. 5. Except for TiO_2, all the samples exhibited two desorption ranges (100–500 °C and 500–900 °C). The desorption range below 500 °C corresponded to the desorption of chemisorption oxygen (O_β), which was considered to be the desorption of oxygen species adsorbed on oxygen vacancies.[25] The desorption range above 500 °C was ascribed to the desorption of lattice oxygen (O_α).[26] The desorption peak temperatures of O_α were almost corresponding to the decomposition temperature of manganese oxide in TG-DSC analysis. The quantities of O_2 desorption of each sample are listed in Table 3. The quantities of low-temperature O_2 desorption peaks (O_β) increased with the loading of MnO_x and CoO_x and then decreased. The desorption
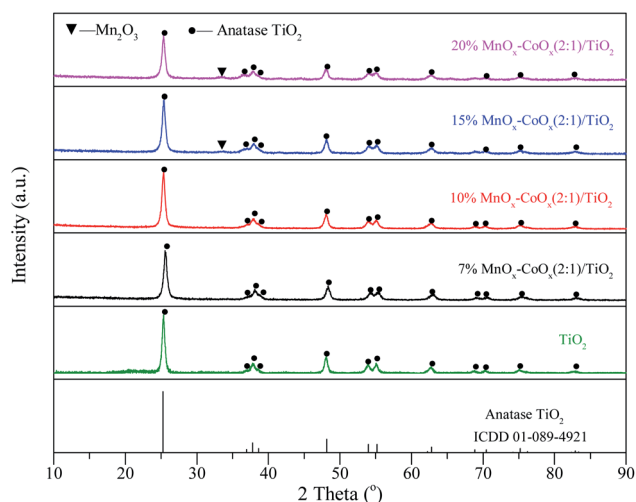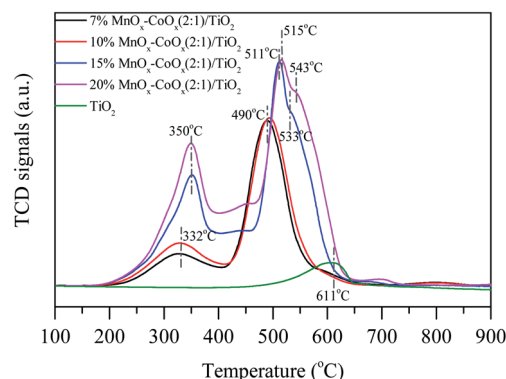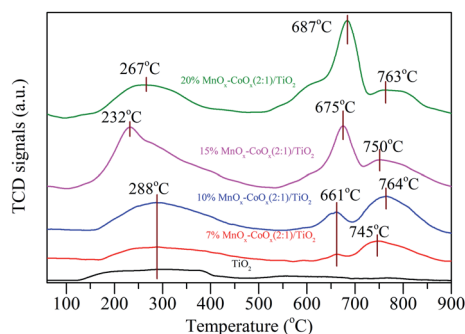

Fig. 3 XRD patterns of catalysts.

Fig. 4 H_2-TPR profiles of catalysts.

Table 2 H$_2$ consumption of H$_2$-TPR

Catalyst	H$_2$ consumption (μmol g^{-1})	
	Low-temperature peak (100–400 °C)	High-temperature peak (400–700 °C)
TiO$_2$	—	29
7%MnO$_x$–CoO$_x$(2 : 1)/TiO$_2$	43	185
10%MnO$_x$–CoO$_x$(2 : 1)/TiO$_2$	59	188
15%MnO$_x$–CoO$_x$(2 : 1)/TiO$_2$	124	245
20%MnO$_x$–CoO$_x$(2 : 1)/TiO$_2$	140	269

Fig. 5 O$_2$-TPD profiles of catalysts.

quantity of chemisorption oxygen (O$_\beta$) of 20%MnO$_x$–CoO$_x$ (2 : 1)/TiO$_2$ was significantly lower than that of 15%MnO$_x$–CoO$_x$(2 : 1)/TiO$_2$. This reflected that 15%MnO$_x$–CoO$_x$(2 : 1)/TiO$_2$ might contain more oxygen vacancies to adsorb O$_2$, so it had the most desorption quantity of oxygen. Moreover, 15%MnO$_x$–CoO$_x$(2 : 1)/TiO$_2$ demonstrated the lowest desorption peak temperature of chemisorption oxygen (O$_\beta$). The lower desorption peak temperature of chemisorption oxygen (O$_\beta$) and the more desorption quantity of O$_\beta$ would be beneficial to the oxidation activity.[27]

3.1.6 NO-TPD analysis. The NO-TPD profiles of the four catalysts and TiO$_2$ carrier are shown in Fig. 6. The desorption peaks of NO had two regions. The desorption peaks below 160 °C could be classified as weakly adsorbed species on the catalyst surface, such as physically adsorbed NO, monodentate nitrates and nitrites. The desorption peaks above 160 °C could be classified as bidentate nitrates and bridged nitrates, which had higher thermal stability.[17,28] The desorption and

decomposition of nitrates and nitrites will be discussed by *in situ* infrared spectroscopy *via* the thermal stability of nitrogen oxides adsorbed on the catalyst. Through NO-TPD profiles, it could be seen that with the increase in loading amount, the peak strength of NO desorption increased first and then decreased slightly, especially for the weakly adsorbed NO below 160 °C. The weakly adsorbed NO desorption peak on 15% MnO$_x$–CoO$_x$(2 : 1)/TiO$_2$ was the largest when compared with other catalysts, indicating that 15%MnO$_x$–CoO$_x$(2 : 1)/TiO$_2$ could adsorb more nitrate and nitrite species and participate in the oxidation reaction of NO, which is helpful to improve the oxidation efficiency of NO.

3.1.7 XPS analysis. The XPS spectra of Mn 2p, Co 2p and O 1s are shown in Fig. 7. In Fig. 7(a), the Mn 2p$_{3/2}$ could be resolved into three sub-bands: Mn^{2+}, Mn^{3+} and Mn^{4+}.[29,30] The binding energies (eV) and valence composition ratios (%) of Mn (Mn^{n+}/Mn) are listed in Table 4. As the loading amount increased, Mn^{2+}/Mn ratio increased first and then decreased; hence, 15%MnO$_x$–CoO$_x$(2 : 1)/TiO$_2$ contained the highest Mn^{2+}/Mn ratio. However, the Mn^{4+}/Mn ratio decreased with the increase in loading while Mn^{3+}/Mn increased. The presence of Mn^{3+} in manganese oxides could promote the formation of oxygen vacancies.[31] The Co 2p in Fig. 7(b) had two main peaks at around 796.0 eV and 780.0 eV, belonging to Co 2p$_{1/2}$ and Co 2p$_{3/2}$, respectively. The satellite peaks at around 785.0–790.0 eV appeared representing the existence of Co^{2+}.[14] The binding energies of Co^{2+} and Co^{3+} are very close, which need to be judged by the split energy level difference of the spin orbits. $\Delta E(2p_{1/2} - 2p_{3/2}) = 16.0$ eV indicates that cobalt ions in the sample is mainly Co^{2+}, while $\Delta E(2p_{1/2} - 2p_{3/2}) = 15.0$ eV indicates that cobalt ions in the sample is mainly Co^{3+}.[14,32] The binding energies (eV), $\Delta E(2p_{1/2} - 2p_{3/2})$ and valence composition ratios (%) of Co (Co^{n+}/Co) are listed in Table 5. $\Delta E(2p_{1/2} -$

Table 3 Quantities of O$_2$ desorption of O$_2$-TPD

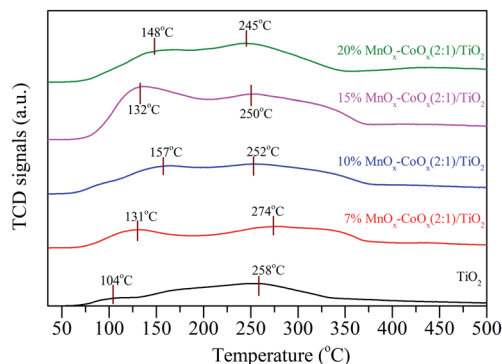| Catalyst	Quantities of O$_2$ desorption (μmol g^{-1})	
	Low-temperature peak (100–500 °C)	High-temperature peak (500–900 °C)
TiO$_2$	6	—
7%MnO$_x$–CoO$_x$(2 : 1)/TiO$_2$	7	8
10%MnO$_x$–CoO$_x$(2 : 1)/TiO$_2$	18	14
15%MnO$_x$–CoO$_x$(2 : 1)/TiO$_2$	31	24
20%MnO$_x$–CoO$_x$(2 : 1)/TiO$_2$	14	43

Fig. 6   NO-TPD profiles of catalysts.

$2p_{3/2}$) of the fresh catalysts were 15.72–15.88 eV, indicating that cobalt ions in these catalysts were mainly Co^{2+}. Therefore, the peaks at around 780.27 eV could be classified as Co^{2+}, and the peaks at around 782.12 eV could be classified as Co^{3+}. As the loading amount increased, $\Delta E(2p_{1/2} - 2p_{3/2})$ decreased first and then increase. It meant that the content of Co^{3+} increased first and then decreased, which corresponded to the Co^{3+}/Co ratio listed in Table 5. Co^{3+}/Co was the highest in 15%MnO_x–$CoO_x(2 : 1)/TiO_2$ among all the catalysts, while the opposite trend was observed for Co^{2+}/Co. Fig. 7(c) shows the XPS spectra of O 1s. The corresponding binding energies (eV) and relative composition ratios (%) are listed in Table 6. The peaks at around 529.89 eV were assigned to lattice oxygen O_α,[33] and the peaks at around 531.55 eV were assigned to oxygen species O_β
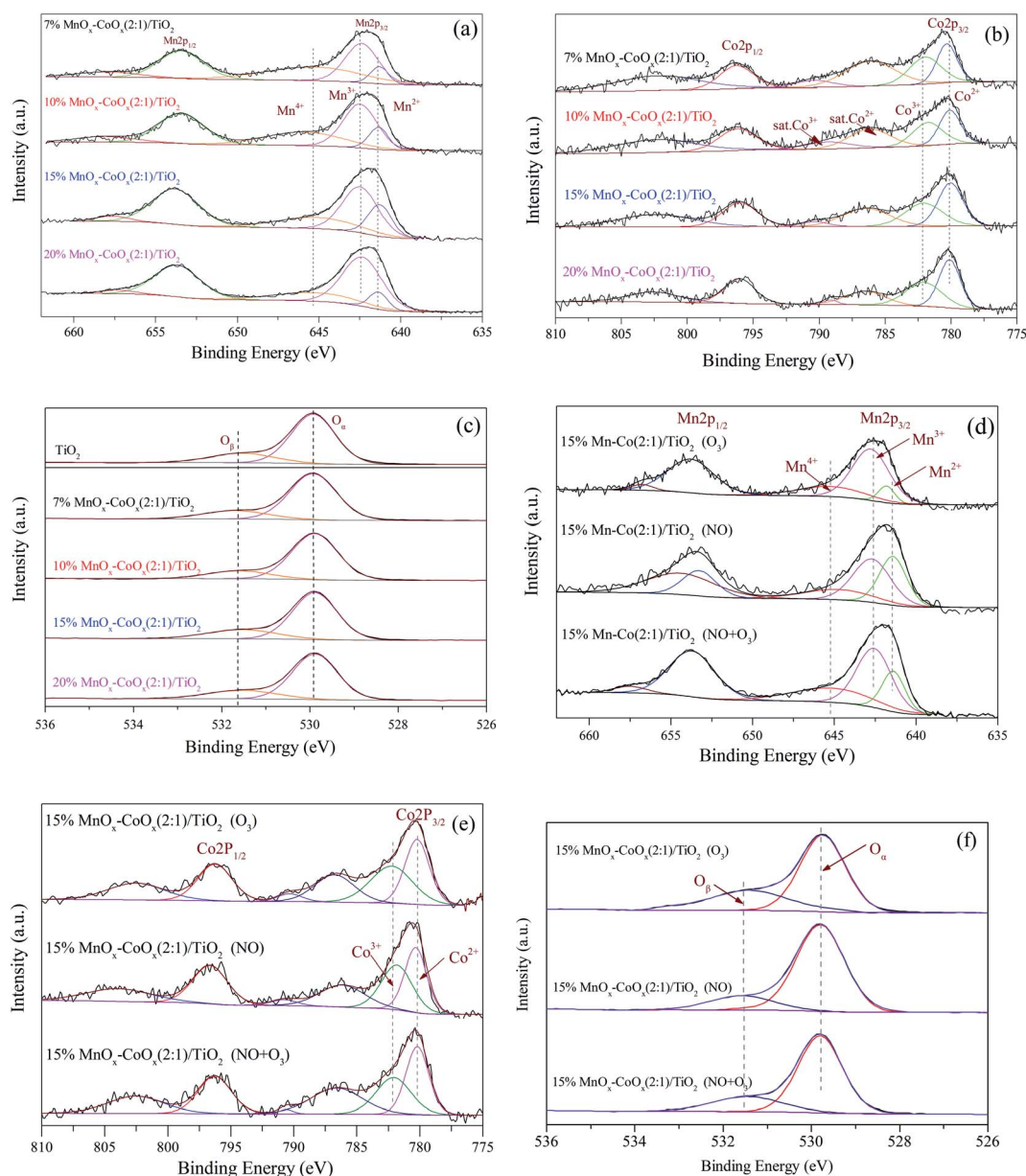

Fig. 7   XPS spectra of catalysts. (a) and (d) Mn 2p; (b) and (e) Co 2p; (c) and (f) O 1s.
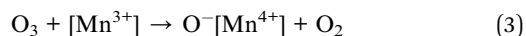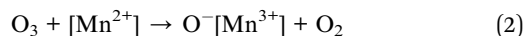
Table 4 Mn $2p_{3/2}$ binding energies (eV) and valence composition (%)

Catalyst	Binding energies (eV)				Valence composition ratios (%)		
	Mn $2p_{3/2}$	Mn^{2+}	Mn^{3+}	Mn^{4+}	Mn^{2+}/Mn	Mn^{3+}/Mn	Mn^{4+}/Mn
$7\%MnO_x–CoO_x(2:1)/TiO_2$	642.08	641.41	642.48	645.34	10.54	44.25	45.21
$10\%MnO_x–CoO_x(2:1)/TiO_2$	642.08	641.42	642.50	645.36	15.18	50.13	34.69
$15\%MnO_x–CoO_x(2:1)/TiO_2$	642.07	641.40	642.50	645.32	17.11	53.39	29.50
$20\%MnO_x–CoO_x(2:1)/TiO_2$	642.07	641.42	642.49	645.32	9.56	67.07	23.37
$15\%MnO_x–CoO_x(2:1)/TiO_2$ (O_3)	642.09	641.44	642.53	645.30	10.71	55.72	33.57
$15\%MnO_x–CoO_x(2:1)/TiO_2$ (NO)	642.07	641.40	642.55	645.28	42.27	46.26	11.47
$15\%MnO_x–CoO_x(2:1)/TiO_2$ $(NO + O_3)$	642.07	641.40	642.51	645.28	16.84	52.77	30.39

which were chemically adsorbed to oxygen vacancies.[34] With the increase in loading of MnO_x and CoO_x, the relative composition ratios of O_α/O decreased first and then increased, while O_β/O increased first and then declined. Consequently, O_β/O was the highest in $15\%MnO_x–CoO_x(2:1)/TiO_2$ among all the catalysts. This variation trend was consistent with the result of O_2-TPD, which confirmed that $15\%MnO_x–CoO_x(2:1)/TiO_2$ contained the largest amount of oxygen vacancies among the four catalysts, and was advantageous to adsorb oxygen species to be used in catalytic oxidation reaction.

The XPS spectra of the used $15\%MnO_x–CoO_x(2:1)/TiO_2$ catalyst after the separate adsorption of O_3 and NO, and the co-adsorption of O_3 and NO at 100 °C are shown in Fig. 7(d)–(f). From Fig. 7(d) and Table 4, it showed that Mn^{2+}/Mn on the surface of 15% Mn–Co(2 : 1)/TiO_2 decreased significantly after O_3 adsorption, while Mn^{3+}/Mn and Mn^{4+}/Mn on the surface of 15% Mn–Co(2 : 1)/TiO_2 increased, which manifested that some of the manganese oxide were probably oxidized by O_3 through eqn (2) and (3).[17] While after NO adsorption, Mn^{3+}/Mn and Mn^{4+}/Mn on the surface of 15% Mn–Co(2 : 1)/TiO_2 decreased, but Mn^{2+}/Mn increased. This illustrated that NO adsorbed on the catalyst probably reacted with manganese oxide in high valence state through eqn (4) and (5).[17] The changes in valence composition ratios of Mn^{2+}/Mn, Mn^{3+}/Mn and Mn^{4+}/Mn on the surface of 15% Mn–Co(2 : 1)/TiO_2 were not significant after NO and O_3 co-adsorbed. It illustrated that the transformations among Mn^{2+}, Mn^{3+} and Mn^{4+} in the NO catalytic oxidation process were almost in balance state. Similarly, Co^{3+}/Co on the

surface of 15% Mn–Co(2 : 1)/TiO_2 increased while Co^{2+}/Co decreased after O_3 adsorption, in Fig. 7(e) and Table 5, which was probably due to the reaction of eqn (6). Co^{2+}/Co increased while Co^{3+}/Co decreased after NO adsorption, which was probably due to the reaction of eqn (7). Simultaneous adsorption of O_3 and NO, the valence composition ratios of Co^{3+}/Co and Co^{2+}/Co were not changed obviously. It also illustrated that the transformations between Co^{3+} and Co^{2+} in the NO catalytic oxidation process were almost in balance state. The relative composition ratio of O_β/O on the surface of 15%Mn–Co(2 : 1)/TiO_2 (in Fig. 7(f) and Table 6) increased after O_3 adsorption. O_β/O decreased slightly after NO adsorption, which may be due to the consumption of chemisorption oxygen by NO reaction on the catalyst surface. After the co-adsorption of NO and O_3, the change in relative composition ratio of O_β/O was not obvious, illustrating that a balance state O_β was set up during this process. It reflected that during the process of NO catalytic oxidation, reactive oxygen species decomposed from O_3 could adsorb on the oxygen vacancies of catalyst, which could supplement the chemisorption oxygen consumed by NO oxidation.
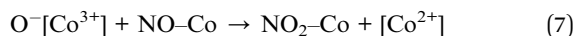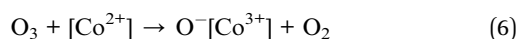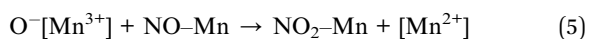
$$O_3 + [Mn^{2+}] \rightarrow O^-[Mn^{3+}] + O_2 \tag{2}$$

$$O_3 + [Mn^{3+}] \rightarrow O^-[Mn^{4+}] + O_2 \tag{3}$$

$$O^-[Mn^{4+}] + NO–Mn \rightarrow NO_2–Mn + [Mn^{3+}] \tag{4}$$

Table 5 Co $2p_{3/2}$ binding energies (eV) and valence composition (%)

Catalyst	Binding energies (eV)				Valence composition ratios (%)	
	Co $2p_{3/2}$	$\Delta E(2p_{1/2} - 2p_{3/2})$	Co^{2+}	Co^{3+}	Co^{2+}/Co	Co^{3+}/Co
$7\%MnO_x–CoO_x(2:1)/TiO_2$	780.91	15.88	780.29	782.08	54.89	45.11
$10\%MnO_x–CoO_x(2:1)/TiO_2$	780.52	15.79	780.27	782.06	53.91	46.09
$15\%MnO_x–CoO_x(2:1)/TiO_2$	780.37	15.72	780.25	782.12	53.66	46.34
$20\%MnO_x–CoO_x(2:1)/TiO_2$	780.22	15.80	780.27	782.12	53.87	46.13
$15\%MnO_x–CoO_x(2:1)/TiO_2$ (O_3)	780.42	15.70	780.30	781.14	50.74	49.26
$15\%MnO_x–CoO_x(2:1)/TiO_2$ (NO)	780.48	15.90	780.32	781.08	56.43	43.57
$15\%MnO_x–CoO_x(2:1)/TiO_2$ $(NO + O_3)$	780.34	15.80	780.27	782.10	54.52	45.48

Table 6 Oxygen species binding energies (eV) and relative composition (%)

Catalyst	Binding energies (eV)			Relative composition ratios (%)	
	O 1s	O_α	O_β	O_α/O	O_β/O
TiO_2	529.91	529.90	531.54	81.05	18.95
$7\%MnO_x–CoO_x(2:1)/TiO_2$	529.91	529.90	531.55	79.99	20.01
$10\%MnO_x–CoO_x(2:1)/TiO_2$	529.90	529.89	531.55	77.27	22.73
$15\%MnO_x–CoO_x(2:1)/TiO_2$	529.90	529.89	531.55	76.62	23.38
$20\%MnO_x–CoO_x(2:1)/TiO_2$	529.90	529.89	531.54	78.20	21.80
$15\%MnO_x–CoO_x(2:1)/TiO_2$ (O_3)	529.90	529.89	531.55	69.36	30.64
$15\%MnO_x–CoO_x(2:1)/TiO_2$ (NO)	529.89	529.90	531.54	79.58	20.42
$15\%MnO_x–CoO_x(2:1)/TiO_2$ (NO + O_3)	529.90	529.89	531.55	75.73	24.27

$$O^-[Mn^{3+}] + NO–Mn \rightarrow NO_2–Mn + [Mn^{2+}] \quad (5)$$

$$O_3 + [Co^{2+}] \rightarrow O^-[Co^{3+}] + O_2 \quad (6)$$

$$O^-[Co^{3+}] + NO–Co \rightarrow NO_2–Co + [Co^{2+}] \quad (7)$$

3.2 NO oxidation properties

The results of NO oxidation efficiencies at different oxidation modes are shown in Fig. 8. With different loadings of MnO_x–$CoO_x(2:1)/TiO_2$, NO oxidation efficiencies first increased with the increase in temperature, reaching the maximum value at 350 °C, and then decreased, as shown in Fig. 8(a). In the H_2-TPR test, the low temperature reduction peak was around 332–350 °C, indicating that at the reaction temperature range of 50–400 °C, the active catalytic components were MnO_2 and Co_3O_4. $15\%MnO_x$–$CoO_x(2:1)/TiO_2$ exhibited the best catalytic efficiency, which can be owned to the best adsorption capacity of oxygen species by the results of O_2-TPD and XPS. For NO oxidation only by O_3, shown in Fig. 8(b), the efficiencies increased with the increase in O_3/NO molar ratio, and decreased rapidly with the increase in temperature. Fig. 8(c) presents the NO oxidation efficiencies using varying loadings of MnO_x–$CoO_x(2:1)/TiO_2$ combined with $O_3/NO = 0.5$. With the increase in temperature, NO oxidation efficiencies increased first (50–100 °C), then decreased (100–300 °C) and again increased from 300 °C to 350 °C, after then decreased again (350–400 °C). Because of the excellent low temperature oxidation performance of ozone and high temperature activity of catalyst, the efficiencies of NO oxidation by ozone combined with catalyst showed this trend with the change in temperature. The introduction of O_3 increased the NO oxidation efficiency, especially at low temperatures (<250 °C), when compared with NO catalytic oxidation by O_2 in Fig. 8(a). This could be ascribed to the good desorption ability of adsorbed oxygen O_β, as seen from the results of O_2-TPD, and the good oxidation performance of O_3 at low temperatures.

N_2 adsorption analysis showed that the specific surface area of the catalysts decreased with the increase in loading capacity. High specific surface area is helpful for the adsorption

performance of the catalyst.[22,35] However, as shown in Fig. 8(a) and (c), NO oxidation efficiencies increased with the total loading from 7% to 15%, which demonstrated that the loading amount or the content of active component was the main factor influencing the catalytic activity when compared to the specific surface area. The NO oxidation efficiency of $20\%MnO_x$–$CoO_x(2:1)/TiO_2$ was slightly lower than that of $15\%MnO_x$–$CoO_x(2:1)/TiO_2$. Although the highest content of Mn^{3+} was found in $20\%MnO_x$–$CoO_x(2:1)/TiO_2$, which was favorable for the formation of oxygen vacancies due to the electrostatic balance,[36] $15\%MnO_x$–$CoO_x(2:1)/TiO_2$ had the highest Co^{3+}/Co and chemisorption oxygen O_β in XPS analysis. It is likely that the interaction of manganese–cobalt produced the most oxygen vacancies at loading amount of 15 wt%, which could adsorb more oxygen species, thereby promoting NO catalytic oxidation.[37,38] Therefore, NO catalytic oxidation efficiency of $15\% MnO_x$–$CoO_x(2:1)/TiO_2$ was slightly higher than that of $20\% MnO_x$–$CoO_x(2:1)/TiO_2$. Fig. 8(d) presents the efficiencies of NO oxidation by O_3 ($O_3/NO = 0.1$–0.9) over $15\%MnO_x$–$CoO_x(2:1)/TiO_2$. Comparing Fig. 8(d) to Fig. 8(b), it was evident that NO oxidation efficiency was improved, especially in the high temperature region (250–400 °C). Therefore, the moderate concentration of $O_3/NO = 0.5$ and $15\%MnO_x$–$CoO_x(2:1)/TiO_2$ were selected as the experimental condition in the following analyses.

The comparisons of NO oxidation efficiencies by different modes are shown in Fig. 8(e) and (f) shows the production of NO_2 by using different oxidation modes. In the experiment, the production of NO_2 was almost corresponding to the oxidation efficiency of NO, indicating that NO_2 was the main products when NO were oxidized by the methods of only using O_2 (4%), only using $15\%MnO_x$–$CoO_x(2:1)/TiO_2$ catalysts, only using O_3 ($O_3/NO = 0.5$), and using $15\%MnO_x$–$CoO_x(2:1)/TiO_2$ combined with O_3 ($O_3/NO = 0.5$). In Fig. 8(e), without O_3 and catalyst, the efficiencies of NO oxidation by O_2 were lower than 5.4%, and decreased with the increase in temperature. This is because NO $+ O_2 \rightarrow NO_2$ is an exothermic reaction and its spontaneous reaction is inefficient at low concentration of O_2.[39] The oxidation efficiency of NO during oxidation by O_3 was much higher than that during catalytic oxidation by O_2 using $15\%MnO_x$–$CoO_x(2:1)/TiO_2$ when the temperature was below 250 °C,
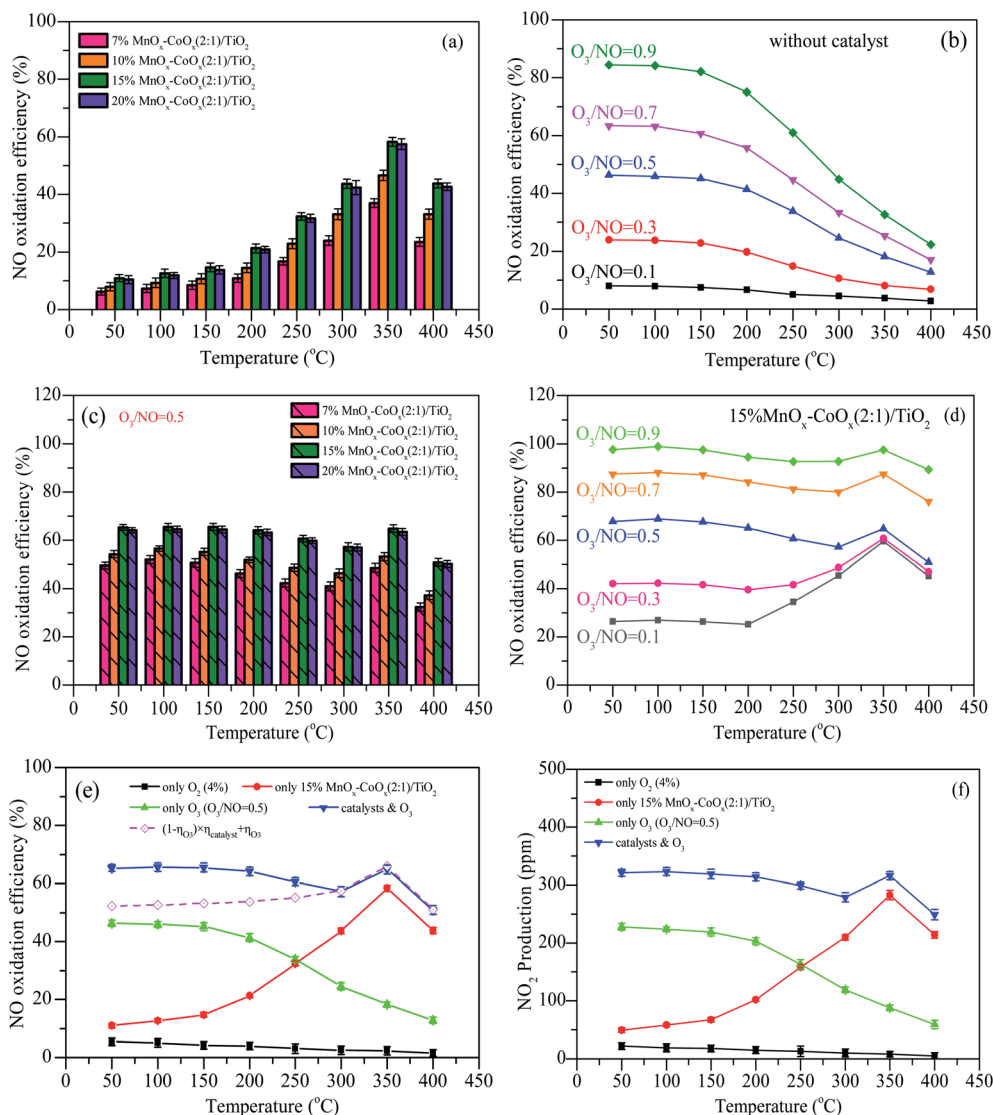
Fig. 8 NO oxidation efficiencies at different oxidation modes. (a) Different loadings of MnO_x–$CoO_x(2 : 1)$/TiO_2; (b) O_3/NO; (c) different loadings of MnO_x–$CoO_x(2 : 1)$/TiO_2 combined with O_3/NO = 0.5; (d) 15%MnO_x–$CoO_x(2 : 1)$/TiO_2 combined with O_3; (e) comparison of NO oxidation by different modes; (f) NO_2 yield by using different oxidation modes. Reaction conditions: flow = 400 mL min^{-1}, NO = 500 ppm, O_2 = 4%, GHSV = 24 000 h^{-1}.

whereas the catalytic reaction occurred more easily above 250 °C. The efficiencies of NO during catalytic oxidation by O_3 using 15%MnO_x–$CoO_x(2 : 1)$/TiO_2 were higher than that during either catalytic oxidation by O_2 using 15%MnO_x–$CoO_x(2 : 1)$/TiO_2 or oxidation by O_3 only. According to the placement of the catalyst in the reactor (Fig. S1†), when NO and O_3 were simultaneously fed into the fixed-bed reactor, NO was first oxidized by O_3, and then the rest of NO was oxidized by O_2 on the catalyst. The theoretical efficiency for combined oxidation was calculated using eqn (8):

$$(1 - \eta_{O_3}) \times \eta_{catalyst} + \eta_{O_3} \qquad (8)$$

where, "η_{O_3}" refers to the NO oxidation efficiency by O_3 and "$\eta_{catalyst}$" represents the NO oxidation efficiency by O_2 using 15%MnO_x–$CoO_x(2 : 1)$/TiO_2.

It can be seen from Fig. 7(e) that the measured efficiencies of NO oxidation by O_3 (O_3/NO = 0.5) using 15%MnO_x–$CoO_x(2 : 1)$/TiO_2 were 5–13% higher than the theoretical efficiencies calculated by eqn (8) below 250 °C, while the measured and theoretical efficiency values were very close above 300 °C. This result indicated that 15%MnO_x–$CoO_x(2 : 1)$/TiO_2 and O_3 exerted a synergistic effect on NO oxidation at temperatures below 250 °C, while the synergistic effect was not evident above 250 °C. The synergistic mechanism between 15%MnO_x–$CoO_x(2 : 1)$/TiO_2 and O_3 and its effect on NO oxidation will be discussed further in the later sections.

3.3 *In situ* DRIFTS studies

Fig. 9 presents the thermal stability of absorbed NO_x species after 15%MnO_x–$CoO_x(2 : 1)$/TiO_2 was exposed to different
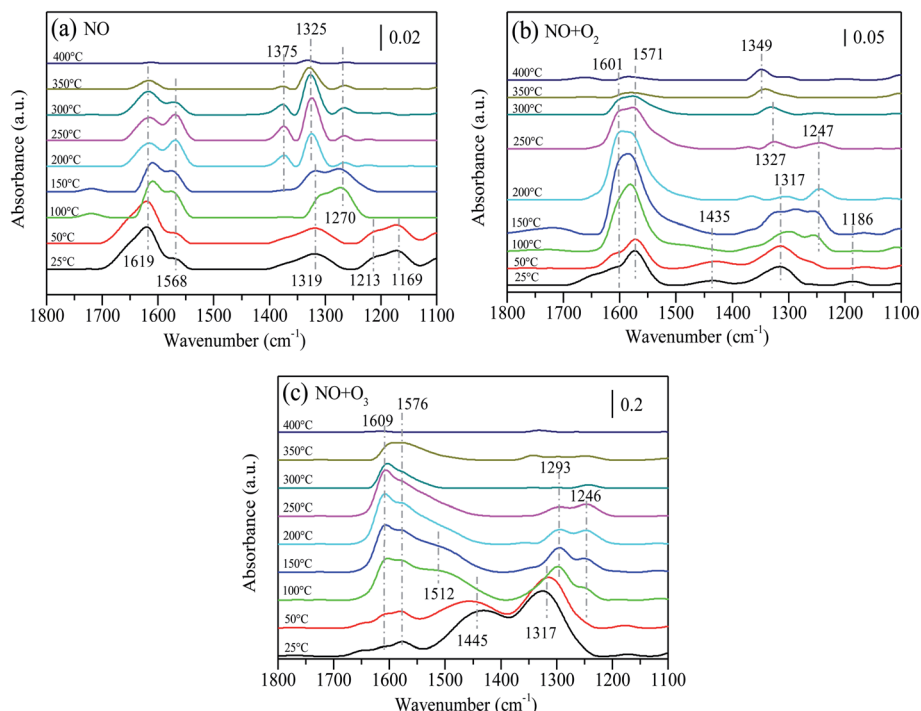
Fig. 9 *In situ* DRIFTS data of absorbed NOₓ species desorption as a function of temperature without fed gases after 15%MnOₓ–CoOₓ(2 : 1)/TiO₂ was exposed to: (a) NO (500 ppm) for 30 min; (b) NO (500 ppm) + O₂ (4%) for 30 min; (c) NO (500 ppm) + O₃ (O₃/NO = 0.5) for 30 min.

atmospheres. The fed gases were adsorbed on the catalyst surface at 25 °C for 30 min, then cut off the fed gases and conducted temperature desorption experiment. After NO adsorbed for 30 min at 25 °C, several peaks appeared at 1619 cm^{-1}, 1568 cm^{-1}, 1319 cm^{-1}, 1213 cm^{-1} and 1169 cm^{-1} on the surface of 15%MnOₓ–CoOₓ(2 : 1)/TiO₂, as shown in Fig. 9(a). The assignments of NOₓ species are listed in Table 7. As the temperature increased, the peak at 1619 cm^{-1} (bridging bidentate nitrates) gradually declined. The band at 1568 cm^{-1} (bidentate nitrates) increased first and then decreased from 250 °C until it disappeared at 350 °C. The bands at 1213 cm^{-1} and 1169 cm^{-1} (nitrites) vanished at 100 °C. The band at 1319 cm^{-1} (nitro–nitrito) gradually increased and shifted to 1270 cm^{-1}. At 100 °C, the peak at 1270 cm^{-1} (monodentate nitrates) appeared and then decreased with the increase in temperature. The bands at 1325 cm^{-1} and 1375 cm^{-1} (nitrate ions) gradually appeared from 200 °C and then declined from 300 °C, disappearing at 400 °C. The above results indicated that

bridging bidentate nitrates, bidentate nitrates, nitro–nitrito, and nitrites were formed at low temperatures, and nitrites were easy to decompose. Bridging bidentate nitrates were decomposed or desorbed with the increase in temperature. The transformation or decomposition of nitro–nitrito and unstable nitrates formed monodentate nitrates and decomposed above 150 °C, while bidentate nitrates were slightly more stable than monodentate nitrates. Nitrate ions gradually accumulated with the conversion of other absorbed NOₓ species, which were thermally stable and did not decompose until above 300 °C.

After 15%MnOₓ–CoOₓ(2 : 1)/TiO₂ co-adsorbed NO and O₂ for 30 min at 25 °C, four peaks appeared at 1601 cm^{-1}, 1571 cm^{-1}, 1435 cm^{-1} 1317 cm^{-1} and 1186 cm^{-1}, as shown in Fig. 9(b). The peaks at 1601 cm^{-1} (bridging bidentate nitrates) and 1571 cm^{-1} (bidentate nitrates) increased with the rise in temperature but started to weaken from 200 °C. The band at 1435 cm^{-1} (monodentate nitrates) disappeared at 150 °C, and the band at 1186 cm^{-1} (nitrites) almost disappeared at 50 °C. The band at

Table 7 Assignments of NO adsorbing species on 15%MnOₓ–CoOₓ(2 : 1)/TiO₂ in *in situ* DRIFTS studies[11,28,32,40–42]

Assignment	Wavenumber (cm^{-1})
Bridging bidentate nitrates	1619, 1609, 1608, 1600, 1602, 1601
Bidentate nitrates	1581, 1578, 1576, 1571, 1568, 1564, 1254, 1252, 1247, 1246, 1245
Monodentate nitrates	1516, 1512, 1445, 1435, 1297, 1293, 1286, 1285, 1270
Nitrate ions	1375, 1365, 1359, 1349, 1331, 1327, 1325,
Nitro–nitrito	1319, 1317
Nitrites	1213, 1203, 1186, 1169, 1167, 1149, 1144

1317 cm^{-1} (nitro–nitrito) moved to high wavenumber and a band at 1247 cm^{-1} (bidentate nitrates) gradually appeared at 100 °C, and then faded away from 200 °C. With the transformation and decomposition of absorbed NO$_x$ species, nitrate ions accumulate gradually at 1327 cm^{-1}, and gradually moved to 1349 cm^{-1}, which did not vanish at 400 °C. Comparing these results to Fig. 9(a), it was inferred that after 15%MnO$_x$–CoO$_x$(2 : 1)/TiO$_2$ was exposed to NO and O$_2$, the desorption of absorbed NO$_x$ species promoted the transformation of other nitrate species to bridging bidentate nitrates and bidentate nitrates, and also increased the accumulation of nitrate ions.

In Fig. 9(c), after 15%MnO$_x$–CoO$_x$(2 : 1)/TiO$_2$ adsorbed NO and O$_3$ for 30 min at 25 °C, four peaks appeared at 1609 cm^{-1}, 1576 cm^{-1}, 1445 cm^{-1} and 1317 cm^{-1}. The very distinct band at 1445 cm^{-1} (monodentate nitrates) increased and shifted to 1512 cm^{-1} as the temperature rose, and was almost covered by the band at 1576 cm^{-1} (bidentate nitrates) at 100 °C. The peaks at 1609 cm^{-1} (bridging bidentate nitrates) and 1576 cm^{-1} (bidentate nitrates) increased with rise in temperature. Nevertheless, the peaks at 1609 cm^{-1} and 1576 cm^{-1} gradually declined above 150 °C. The band at 1317 cm^{-1} (nitro–nitrito) moved to 1293 cm^{-1} (monodentate nitrates) with the rise in temperature and declined from 150 °C. Moreover, the band at 1246 cm^{-1} (bidentate nitrates) appeared at 100 °C and declined from 150 °C. The decomposition rate of monodentate nitrates was faster than that of bidentate nitrates. Comparing Fig. 9(a) and (b), it can be seen that the desorption of absorbed NO$_x$ species, after 15%MnO$_x$–CoO$_x$(2 : 1)/TiO$_2$ was exposed to NO and O$_3$, promoted the generation and transformation of monodentate nitrates and inhibited the formation of nitrate ions. Except for monodentate nitrates and nitrites at 1144–1213 cm^{-1}, the decomposition of other absorbed NO$_x$ species in Fig. 9(a) and (b) occurred at 200 °C or more, but the decomposition occurred at 150 °C in Fig. 9(c). Therefore, NO oxidation by O$_3$ combined with 15%MnO$_x$–CoO$_x$(2 : 1)/TiO$_2$ lowered the transformation and decomposition temperature of absorbed NO$_x$ species, and inhibited the aggregation of nitrate ions on the catalyst surface. These effects were beneficial to the oxidation of NO.

In situ DRIFTS studies of NO$_x$ adsorbed on 15%MnO$_x$–CoO$_x$(2 : 1)/TiO$_2$ as a function of time were performed to reveal the effect of synergistic mechanism between 15%MnO$_x$–CoO$_x$(2 : 1)/TiO$_2$ and O$_3$ on NO oxidation. The fed gases were continued to introduce into the reaction cell for 1 h, and the infrared absorption spectra were recorded at intervals of one minute. Fig. 10(a) shows the temporal evolution of in situ DRIFTS curve during NO oxidation by O$_2$ on 15%MnO$_x$–CoO$_x$(2 : 1)/TiO$_2$ at 100 °C (NO = 500 ppm, O$_2$ = 4%). After NO and O$_2$ were introduced together into the DRIFTS cell, there was gradual appearance of peaks at 1609 cm^{-1} (bridging bidentate nitrates), 1581 cm^{-1} (bidentate nitrates), 1331 cm^{-1} (nitrate ions), 1254 cm^{-1} (bidentate nitrates), 1286 cm^{-1} (monodentate nitrates), and 1203 cm^{-1} (nitrites). The in situ DRIFTS curves in the range of 1100–1800 cm^{-1} were fitted by Gauss function to obtain the area of each sub-peak (for example, the sub-peaks at 1609 cm^{-1}, 1581 cm^{-1}, 1331 cm^{-1}, 1286 cm^{-1}, 1254 cm^{-1} and 1203 cm^{-1}). The maximum area of each sub-peak during the

first 30 minutes of reaction time was chosen as the standard. The relative intensity of each band was obtained by comparing the band area to the standard area. The slope of each relative intensity curve represented the rate of production or decomposition of each species. It can be seen clearly in Fig. 10(b) that the relative intensity of the peaks at 1609 cm^{-1}, 1331 cm^{-1} and 1286 cm^{-1} progressively increased. Moreover, the peaks at 1581 cm^{-1} and 1254 cm^{-1} increased rapidly from 10 min and outpaced the other nitrate species. However, the peak at 1203 cm^{-1} appeared quickly within 3 min, and then declined especially after 10 min. These results indicated that nitrites were transformed or decomposed, which accelerated the production of bidentate nitrates.

Fig. 10(c) shows the in situ DRIFTS curves during NO oxidation by O$_3$ on 15%MnO$_x$–CoO$_x$(2 : 1)/TiO$_2$ at 100 °C (NO = 500 ppm, O$_2$ = 4%, O$_3$/NO = 0.5). The peaks at 1608 cm^{-1} (bridging bidentate nitrates), 1578 cm^{-1} (bidentate nitrates), 1516 cm^{-1} (monodentate nitrates), 1297 cm^{-1} (monodentate nitrates) and 1254 cm^{-1} (bridging bidentate nitrates) appeared gradually. No characteristic peaks of nitrate ions and nitrites appeared which were consistent with the thermal stability test in Fig. 9(c). A new band appeared at 1516 cm^{-1} (monodentate nitrates) in the O$_3$ oxidation system at 100 °C compared to Fig. 10(a). The intensity of the peak at 1608 cm^{-1} was higher than that of 1578 cm^{-1} and intensity of the peak at 1297 cm^{-1} was higher than that of 1254 cm^{-1} in Fig. 10(c) when compared with Fig. 10(a). This might due to that O$_3$ accelerated the generation of bridging bidentate nitrates at 1608 cm^{-1}, which promoted the production of monodentate nitrates at 1516 cm^{-1} and 1297 cm^{-1}. The relative intensities of all species increased significantly within 10 min in Fig. 10(d), and then closed to adsorption saturation. By comparing the relative intensities in Fig. 10(b) and (d), it can be concluded that the oxidation of NO by O$_3$ was much stronger than that by O$_2$ on 15%MnO$_x$–CoO$_x$(2 : 1)/TiO$_2$ at 100 °C.

Fig. 10(e) shows the in situ DRIFTS curves during NO oxidation by O$_2$ on 15%MnO$_x$–CoO$_x$(2 : 1)/TiO$_2$ at 350 °C (NO = 500 ppm, O$_2$ = 4%). There were seven major bands located at 1600 cm^{-1} (bridging bidentate nitrates), 1564 cm^{-1} (bidentate nitrates), 1359 cm^{-1} (nitrate ion), 1286 cm^{-1} (monodentate nitrates), 1252 cm^{-1} (bidentate nitrates), 1169 cm^{-1} and 1144 cm^{-1} (nitrites). When NO and O$_2$ were simultaneously injected into DRIFTS cell at 350 °C, all the bands appeared quickly within 1 min, but did not increase significantly thereafter. This indicated that the reaction of NO and O$_2$ on the surface of 15%MnO$_x$–CoO$_x$(2 : 1)/TiO$_2$ at 350 °C was rapid. Fig. 10(f) shows the relative intensity of each band. It can be seen that the relative intensities of all the species remained greater than 60%, indicating that the accumulation and decomposition of all the intermediate products were in dynamic equilibrium.

Fig. 10(g) presents the in situ DRIFTS curves during NO oxidation by O$_3$ on 15%MnO$_x$–CoO$_x$(2 : 1)/TiO$_2$ at 350 °C (NO = 500 ppm, O$_2$ = 4%, O$_3$/NO = 0.5). Similar to Fig. 10(e), seven peaks appeared within 1 min, including 1602 cm^{-1} (bridging bidentate nitrates), 1578 cm^{-1} (bidentate nitrates), 1365 cm^{-1} (nitrate ion), 1285 cm^{-1} (monodentate nitrates), 1245 cm^{-1}
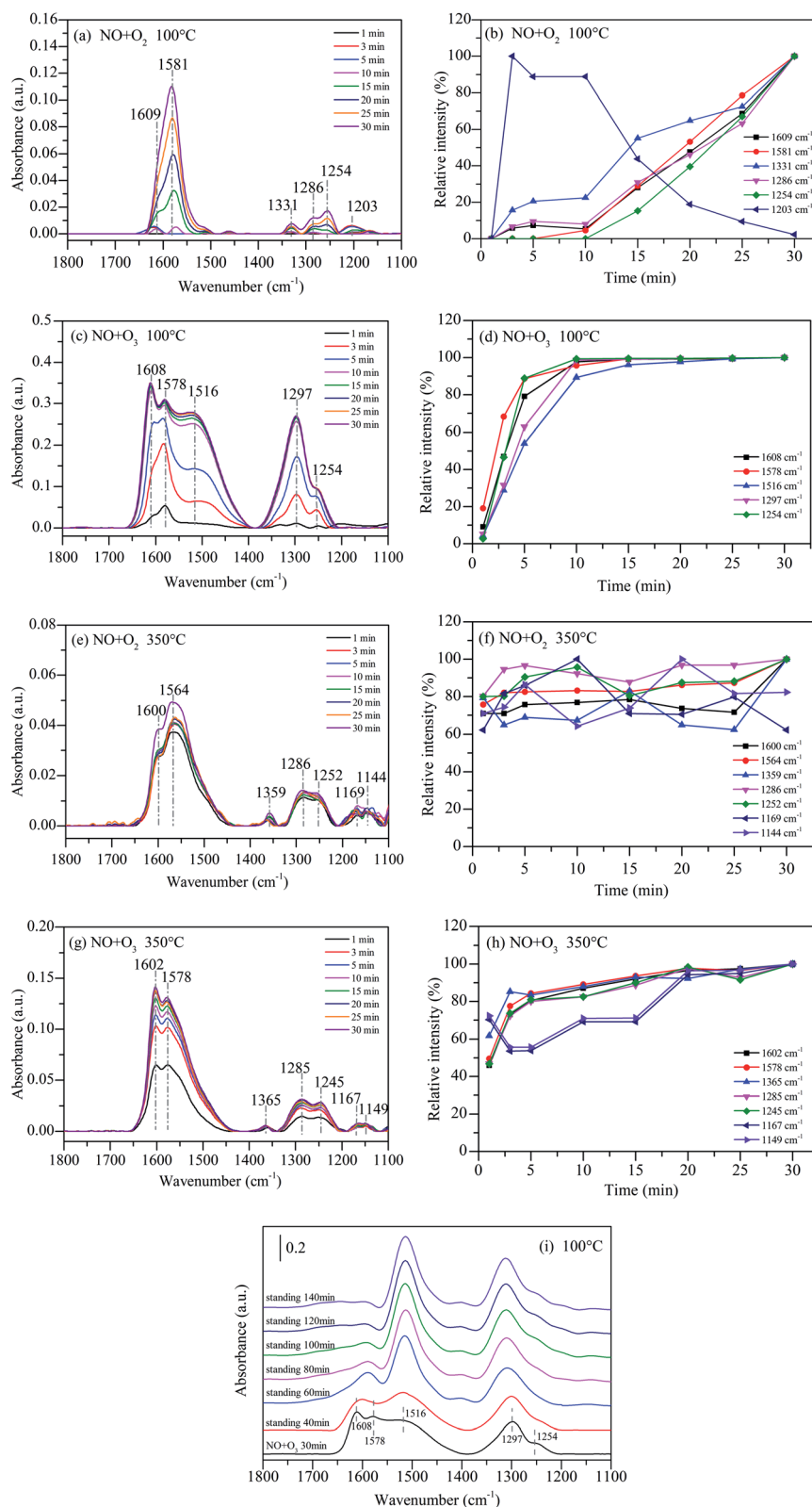
Fig. 10 *In situ* DRIFTS data of NO adsorbed on 15%MnO$_x$–CoO$_x$(2 : 1)/TiO$_2$ as a function of time: (a) NO + O$_2$ at 100 °C; (b) relative intensity of NO + O$_2$ at 100 °C; (c) NO + O$_3$ at 100 °C; (d) relative intensity of NO + O$_3$ at 100 °C; (e) NO + O$_2$ at 350 °C; (f) relative intensity of NO + O$_2$ at 350 °C; (g) NO + O$_3$ at 350 °C; (h) relative intensity of NO + O$_3$ at 350 °C; (i) static reaction after NO and O$_3$ adsorbed at 100 °C.

(bidentate nitrates), 1167 cm^{-1} and 1149 cm^{-1} (nitrites). The relative intensity of each intermediate species is presented in Fig. 10(h). All the bands in the presence of O$_3$ at 350 °C rapidly

generated but then grew slowly. Therefore, it can be concluded that the effect of ozone on the intermediates formed during catalytic oxidation was weakened at high temperature, but it
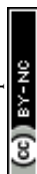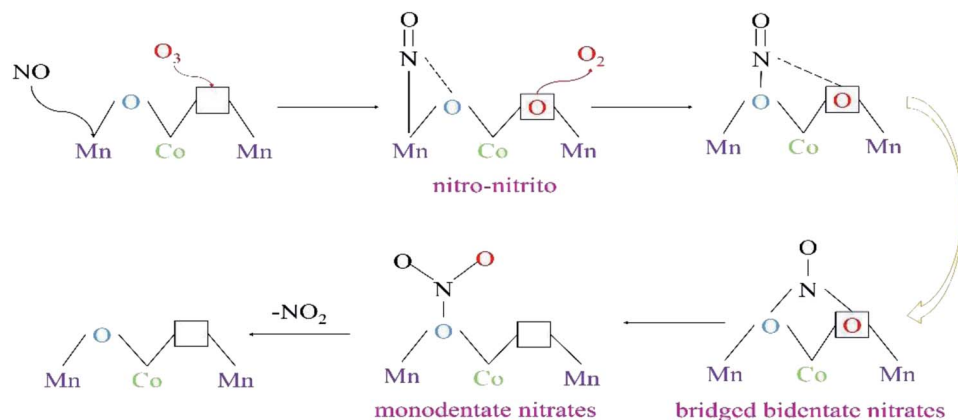
Fig. 11 The pathway of NO oxidation by O_3 (O_3/NO < 1) over 15%MnO_x–CoO_x(2 : 1)/TiO_2.

still enhanced the NO catalytic oxidation. In addition, the peaks at 1167 cm^{-1} and 1149 cm^{-1} fluctuated greatly, indicating that there was partial decomposition of nitrites at 350 °C compared to that at 100 °C. Comparing the reaction of NO catalytic oxidation by O_3 on 15%MnO_x–CoO_x(2 : 1)/TiO_2 at 100 °C (Fig. 10(c)), there was no significant increase in monodentate nitrates around 1516 cm^{-1} and 1297 cm^{-1} during NO oxidation by O_2 or O_3 on 15%MnO_x–CoO_x(2 : 1)/TiO_2 at 350 °C (Fig. 10(e) and (g)). In combination with the results of catalyst activity test, it was evident that the synergistic effect appeared only during NO oxidation by O_3 (O_3/NO = 0.5) on 15%MnO_x–CoO_x(2 : 1)/TiO_2 below 250 °C (Fig. 8(e)). Thus, it can be speculated that monodentate nitrates were the pivotal intermediate products involved in the synergistic effect promoting the NO catalytic oxidation.

Fig. 10(i) presents the static reaction after NO and O_3 co-adsorbed at 100 °C on 15%MnO_x–CoO_x(2 : 1)/TiO_2. The peaks at 1608 cm^{-1} (bridging bidentate nitrates), 1578 cm^{-1} (bidentate nitrates), 1516 cm^{-1} (monodentate nitrates), 1297 cm^{-1} (monodentate nitrates) and 1254 cm^{-1} (bidentate nitrates) formed after NO and O_3 co-adsorbed at 100 °C for 30 min. When all the gases were cut off and the adsorbed catalyst was left to stand for a period, the changes in the infrared absorption peaks of nitrate species were recorded. With the extension of the standing time, the characteristic peaks of bridging bidentate nitrates and bidentate nitrates at around 1608–1578 cm^{-1} were significantly reduced, while the characteristic peaks of mono-dentate nitrates at 1516 cm^{-1} and 1297 cm^{-1} were enhanced, and the peak at 1254 cm^{-1} was covered by the peak at 1297 cm^{-1}. This indicated that bridging bidentate nitrates and bidentate nitrates could convert to monodentate nitrates.

From the *in situ* DRIFTS tests of NO$_x$ desorption with increase in temperature, and the tests of NO oxidation by O_3 or O_2 using 15%MnO_x–CoO_x(2 : 1)/TiO_2 at 100 °C and 350 °C, the transformations occurring between bridging bidentate nitrates, bidentate nitrates, monodentate nitrates and nitro–nitrito were determined. The results of characterization analyses showed that 15%MnO_x–CoO_x(2 : 1)/TiO_2 contained oxygen vacancies, which could promote O_3 to decompose an active oxygen atom at oxygen vacancy and desorbed an oxygen molecule.[43] After NO

reacted with active oxygen atom forming NO_2, the oxygen vacancy was available to adsorb the next active oxygen atom.[17] The pathway of NO catalytic oxidation by O_3 using 15%MnO_x–CoO_x(2 : 1)/TiO_2 is depicted in Fig. 11 and "□" represents oxygen vacancy.

In the *in situ* DRIFTS results of NO$_x$ desorption shown in Fig. 9, nitro–nitrito was formed on the surface of 15%MnO_x–CoO_x(2 : 1)/TiO_2 after NO was adsorbed at 25 °C. Therefore, NO was adsorbed on the active metal atom of the catalyst to form nitro–nitrito, which then reacted with the adsorbed oxygen to form other nitrate species. The rise in reaction temperature accelerated the transformation and decomposition of nitrate species, leading to the increase in NO oxidation efficiency. However, in the *in situ* DRIFTS curves of NO oxidation by O_3 on 15%MnO_x–CoO_x(2 : 1)/TiO_2 at 100 °C (Fig. 10(c)), nitro–nitrito could not be observed. This was because it transformed to other nitrate species at 100 °C (Fig. 9(c)), especially to monodentate nitrates. Mass-produced monodentate nitrates could decompose into gaseous NO_2, facilitating the oxidation of NO to NO_2. This could be the reason for the synergistic effect on NO oxidation by O_3 using 15%MnO_x–CoO_x(2 : 1)/TiO_2 at low temperature.

4. Conclusions

In this work, TiO_2-supported catalysts with various loading amounts of MnO_x–CoO_x (molar ratio of Mn to Co = 2 : 1) were prepared and evaluated in the oxidation of NO in presence of low ratio of O_3 (O_3/NO < 1). It was found that 15%MnO_x–CoO_x(2 : 1)/TiO_2 displayed the optimal catalytic oxidation of NO due to its good redox performance, high surface oxygen mobility, most oxygen vacancies and chemisorbed oxygen. The NO oxidation efficiency was increased by O_3 (O_3/NO < 1) combined with 15%MnO_x–CoO_x(2 : 1)/TiO_2 at 50–400 °C, especially below 250 °C. The synergistic effect of NO oxidation efficiency in the presence of O_3 (O_3/NO < 1) over 15%MnO_x–CoO_x(2 : 1)/TiO_2 was observed below 250 °C. The results of *in situ* DRIFTS studies confirmed that O_3 accelerated the transition between nitrate species, reduced the decomposition temperature of nitrate species, speeded up the rate of NO oxidation and

inhibited the formation of nitrate ions. Below 250 °C, the mass-produced monodentate nitrates were responsible for the synergistic enhancement when both 15%MnO_x–CoO_x(2 : 1)/TiO_2 and O_3 were present. This conclusion can provide theoretical basis for the study of NO catalytic oxidation by low concentration ozone in the future.

Conflicts of interest

There are no conflicts to declare.

Acknowledgements

References

1 D. Damma, P. R. Ettireddy, B. M. Reddy and P. G. Smirniotis, *Catalysts*, 2019, **9**(4), 349.

2 J. Yang, Z. Su, S. Ren, H. Long, M. Kong and L. Jiang, *J. Energy Inst.*, 2019, **92**, 883–891.

3 M. Mladenović, M. Paprika and A. Marinković, *Renewable Sustainable Energy Rev.*, 2018, **82**, 3350–3364.

4 C. Chen, Y. Cao, S. Liu, J. Chen and W. Jia, *Chin. J. Catal.*, 2018, **39**, 1347–1365.

5 I. Jõgi, E. Stamate, C. Irimiea, M. Schmidt, R. Brandenburg, M. Hołub, M. Bonisławski, T. Jakubowski, M.-L. Kääriäinen and D. C. Cameron, *Fuel*, 2015, **144**, 137–144.

6 Q. Ma, Z. Wang, F. Lin, M. Kuang, R. Whiddon, Y. He and J. Liu, *Energy Fuels*, 2016, **30**, 2302–2308.

7 Q. Wu, C. Sun, H. Wang, T. Wang, Y. Wang and Z. Wu, *Chem. Eng. J.*, 2018, **341**, 157–163.

8 H. T. Li, F. Liu, S. H. Wang, F. J. Wang, X. Qian, C. D. Zhang, Y. L. Ma and L. D. Wang, *Fuel Process. Technol.*, 2019, **194**, 106125.

9 K. Li, X. Tang, H. Yi, P. Ning, D. Kang and C. Wang, *Chem. Eng. J.*, 2012, **192**, 99–104.

10 E. Park, S. Chin, J. Jeong and J. Jurng, *Microporous Mesoporous Mater.*, 2012, **163**, 96–101.

11 G. Qi and W. Li, *Catal. Today*, 2015, **258**, 205–213.

12 D. Shang, Q. Zhong and W. Cai, *Appl. Surf. Sci.*, 2015, **325**, 211–216.

13 L. Qiu, Y. Wang, D. Pang, F. Ouyang, C. Zhang and G. Cao, *Catalysts*, 2016, **6**, 9.

14 H. Li, S. Wang, X. Wang, N. Tang, S. Pan and J. Hu, *Fuel*, 2017, **202**, 470–482.

15 K. Skalska, J. S. Miller and S. Ledakowicz, *Sci. Total Environ.*, 2010, **408**, 3976–3989.

16 I. Jõgi, K. Erme, J. Raud and M. Laan, *Fuel*, 2016, **173**, 45–51.

17 F. Lin, Z. Wang, Q. Ma, Y. Yang, R. Whiddon, Y. Zhu and K. Cen, *Appl. Catal., B*, 2016, **198**, 100–111.

18 C. Han, S. Zhang, L. Guo, Y. Zeng, X. Li, Z. Shi, Y. Zhang, B. Zhang and Q. Zhong, *Chem. Eng. Res. Des.*, 2018, **136**, 219–229.

19 D. Fang, J. Xie, H. Hu, H. Yang, F. He and Z. Fu, *Chem. Eng. J.*, 2015, **271**, 23–30.

20 L. J. Swain B and C. G. Lee, *Arch. Metall. Mater.*, 2018, **63**, 1037–1042.

21 J. Xie, D. Fang, F. He, J. Chen, Z. Fu and X. Chen, *Catal. Commun.*, 2012, **28**, 77–81.

22 X. Zhang, B. Shen, F. Shen, X. Zhang, M. Si and P. Yuan, *Chem. Eng. J.*, 2017, **326**, 551–560.

23 J. Han, D. Wang, Y. Du, S. Xi, J. Hong, S. Yin, Z. Chen, T. Zhou and R. Xu, *J. Mater. Chem. A*, 2015, **3**, 20607–20613.

24 J. Li, L. Li, W. Cheng, F. Wu, X. Lu and Z. Li, *Chem. Eng. J.*, 2014, **244**, 59–67.

25 Q. Liang, X. Wu, D. Weng and H. Xu, *Catal. Today*, 2008, **139**, 113–118.

26 W. Li, C. Zhang, X. Li, P. Tan, A. Zhou, Q. Fang and G. Chen, *Chin. J. Catal.*, 2018, **39**, 1653–1663.

27 F. Gao, X. Tang, H. Yi, C. Chu, N. Li, J. Li and S. Zhao, *Chem. Eng. J.*, 2017, **322**, 525–537.

28 D. Meng, W. Zhan, Y. Guo, Y. Guo, L. Wang and G. Lu, *ACS Catal.*, 2015, **5**, 5973–5983.

29 P. Sudarsanam, B. Hillary, M. H. Amin, S. B. A. Hamid and S. K. Bhargava, *Appl. Catal., B*, 2016, **185**, 213–224.

30 W. Tang, X. Wu, S. Li, X. Shan, G. Liu and Y. Chen, *Appl. Catal., B*, 2015, **162**, 110–121.

31 M. Si, B. X. Shen, H. H. Zhang, L. J. Liu, W. J. Zhou, Z. Liu, Y. J. Pan and X. Zhang, *Ind. Eng. Chem. Res.*, 2020, **59**, 1467–1476.

32 H. Hu, S. Cai, H. Li, L. Huang, L. Shi and D. Zhang, *J. Phys. Chem. C*, 2015, **119**, 22924–22933.

33 A. Chalkidis, D. Jampaiah, P. G. Hartley, Y. M. Sabri and S. K. Bhargava, *Fuel Process. Technol.*, 2019, **193**, 317–327.

34 W. Fan, H. Li, F. Zhao, X. Xiao, Y. Huang, H. Ji and Y. Tong, *Chem. Commun.*, 2016, **52**, 5316–5319.

35 X. Zhang, B. Shen, X. Zhang, F. Wang, G. Chi and M. Si, *RSC Adv.*, 2017, **7**, 5928–5936.

36 F. Wang, H. Dai, J. Deng, G. Bai, K. Ji and Y. Liu, *Environ. Sci. Technol.*, 2012, **46**, 4034–4041.

37 B. Meng, Z. Zhao, X. Wang, J. Liang and J. Qiu, *Appl. Catal., B*, 2013, **129**, 491–500.

38 L. Zhang, L. Shi, L. Huang, J. Zhang, R. Gao and D. Zhang, *ACS Catal.*, 2014, **4**, 1753–1763.

39 F. Lin, Z. Wang, Z. Zhang, Y. He, Y. Zhu, J. Shao, D. Yuan, G. Chen and K. Cen, *Chem. Eng. J.*, 2019, **382**, 123030.

40 H. Hu, K. Zha, H. Li, L. Shi and D. Zhang, *Appl. Surf. Sci.*, 2016, **387**, 921–928.

41 Y. Yu, J. Wang, J. Chen, X. Meng, Y. Chen and C. He, *Ind. Eng. Chem. Res.*, 2014, **53**, 16229–16234.

42 N. Tang, Y. Liu, H. Wang and Z. Wu, *J. Phys. Chem. C*, 2011, **115**, 8214–8220.

43 V. P. Santos, M. F. R. Pereira, J. J. M. Órfão and J. L. Figueiredo, *Appl. Catal., B*, 2010, **99**, 353–363.